Check for updates

A direct *Z*-scheme Bi₂WO₆/NH₂–UiO-66 nanocomposite as an efficient visible-light-driven photocatalyst for NO removal†

Yiqiu Liu,[ab] Yi Zhou,[ab] Qijun Tang,[ab] Qian Li,[ab] Si Chen,[ab] Zhuxing Sun[c] and Haiqiang Wang [iD] *[ab]

To explore an efficient photocatalyst for NO pollution, a direct *Z*-scheme photocatalytic system is successfully fabricated by coupling Bi₂WO₆ with NH₂-UiO-66 *via* a simple hydrothermal synthesis technique. The *Z*-scheme system promotes the NO photocatalytic oxidation activity with an optimum NO removal rate of 79%, which is 2.7 and 1.2 times that obtained by using only pristine Bi₂WO₆ and NH₂-UiO-66, respectively. Simultaneously, superior selectivity for converting NO to NO_3^-/NO_2^- is observed. The enhanced photocatalytic performance of the Bi₂WO₆/NH₂-UiO-66 hybrids is attributed to the following two aspects: (i) large specific area of NH₂-UiO-66, which exposes more active sites and is beneficial to the adsorption and activation of NO; (ii) outstanding *Z*-scheme structure constructed between BiWO₆ and NH₂-UiO-66, which can improve the efficiency of the separation of electron–hole pairs and preserves the strong oxidation ability of hybrids. ESR analysis shows that $\cdot O_2^-$ and $\cdot OH$ contribute to NO removal. A possible photocatalytic mechanism of NO oxidation on the direct *Z*-scheme photocatalyst (BWO/2NU) under visible light irradiation is proposed. This work displays the BWO/2NU hybrid's potential for treating low-concentration air pollutants, and the proposed *Z*-scheme photocatalyst design and promotion mechanism may inspire more rational synthesis of highly efficient photocatalysts for NO removal.

1. Introduction

Rapid industrialization and urbanization have led to a sharp increase in harmful gas emissions, such as volatile organic compounds (VOCs) and nitrogen oxides (NO$_x$), which have become the most significant pollutants in prominent environmental issues.[1,2] NO is a typical air pollutant and results in many hazards, such as tropospheric ozone depletion, global climate warming, acid rain, and human diseases.[3] Different techniques including physical and chemical adsorption,[4] heterogeneous catalytic reduction,[5] and oxidation and so on[6] are usually adopted to eliminate NO from gas emissions from combustion sources. However, these technologies are usually employed to treat NO at relatively high concentrations.[7] For practical ppb-level NO, it widely exists in both indoor and outdoor atmospheric environments, which has severe impacts on ecology and human health. Photocatalytic oxidation appears to be an environment friendly and easy approach to removing NO at ppb levels in air.[3,8,9]

Among the various reported photocatalysts, it's difficult for a single-component material to achieve superior performance, including stability, effective separation of photogenerated charges, utilization efficiency of solar energy and strong redox ability.[10] Therefore, a variety of strategies have been developed and applied to improve the performance of single-component materials, such as size and morphology control,[11] surface modification,[12] defect engineering[13] and heterojunction construction.[14] Among them, the constructed heterojunctions are promising due to high separation efficiency of electron–hole pairs, including type II heterojunctions and *Z*-scheme photocatalysts and so on. In comparison with type II heterojunctions, *Z*-scheme photocatalytic system can minimize unfavorable backward reaction at two different redox sites during the photocatalytic process[15] and preserve the higher redox potentials of the photo-induced charges, showing excellent photocatalytic performance.[14,16–18] Thus, direct *Z*-scheme photocatalysts have been studied and applied,[15,16,19,20] ever since Yu *et al.* pioneered the direct *Z*-scheme photocatalyst g–C₃N₄–TiO₂ and applied it to decompose formaldehyde in air.[21]

[a]Key Laboratory of Environment Remediation and Ecological Health, Ministry of Education, College of Environmental & Resources Science, Zhejiang University, Hangzhou 310058, P. R. China. E-mail: haiqiangwang@zju.edu.cn; Fax: +86-571-87953088; Tel: +86-571-87953088

[b]Zhejiang Provincial Engineering Research Center of Industrial Boiler & Furnace Flue Gas Pollution Control, Hangzhou, 311202, P. R. China

[c]School of Environmental Science and Engineering, Shanghai Jiao Tong University, Shanghai 200240, China

† Electronic supplementary information (ESI) available. See DOI: 10.1039/c9ra09270f

Bismuth tungstate (Bi_2WO_6), an environment-friendly material, has been widely studied and applied in photocatalysis owing to its unique properties, such as nontoxicity, a visible light response range and a regulable band gap of 2.75 eV.[22] Moreover, its unique band structure makes the valence band largely dispersed and does benefits to the mobility of photo-induced carriers.[23] However, a few drawbacks limit the photocatalytic performance of Bi_2WO_6, including high recombination of photoinduced electron–hole pairs and low utilization of visible light.[24] Therefore, it is imperative to overcome these disadvantages. Coupling Bi_2WO_6 with other materials to construct Z-scheme heterojunction photocatalysts could help achieve this objective. For example, Hu et al.[25] designed and synthesized a Z-scheme photocatalytic system (2D/2D BP/monolayer Bi_2WO_6). The Z-scheme photocatalyst showed superior performance in photocatalytic water splitting and photocatalytic NO removal. And the NO removal ratio was as high as 67%.

NH_2-UiO-66, a typical metal–organic frameworks (MOFs) material, have been widely applied in different areas owing to their high specific surface areas, tailorable pore sizes, easy functional groups, stability and designed frame structures.[26] Combing NH_2-UiO-66 with Bi_2WO_6 can provide extra pathways for the charge migration and facilitate the efficient separation of photo-induced carriers. In addition, the incorporation may lead to the formation of a Z-scheme photocatalytic system and maintaining high redox potential, which are beneficial for good catalytic activity and selectivity.[27]

Here, we constructed a novel direct Z-scheme photocatalyst to promote NO removal and selectivity at a ppb level under visible light irradiation in a continuous gas flow. In our work, Bi_2WO_6 and NH_2-UiO-66 were chosen to form an interactive interface between them via a simple hydrothermal method, and a novel direct Z-scheme system, Bi_2WO_6/xNH_2-UiO-66 (BWO/xNU), was fabricated. On the one hand, bismuth tungstate (Bi_2WO_6), an environment-friendly material, is being extensively studied for photocatalysis owing to unique properties. NH_2-UiO-66 displays superior features in owing to large surface areas, high stability, visible-light response, and semiconductor properties.[27–31] One the other hand, the band position of NH_2-UiO-66 matched well with that of Bi_2WO_6. Combining NH_2-UiO-66 with Bi_2WO_6 can lead to forming a Z-scheme band structure, which ensures high separation efficiency of photogenerated electrons and holes. More importantly, the BWO/xNU hybrids can preserve the strong oxidation ability on the valence band (VB) of NH_2-UiO-66 and high reduction ability on the conduction band (CB) of Bi_2WO_6 simultaneously. The as-prepared BWO/xNU hybrids exhibited both higher photocatalytic ability for NO oxidation and improved selectivity for NO_3^-/NO_2^- conversion. Hence, this work provides a basis for designing a MOFs-based direct Z-scheme photocatalytic system, simultaneously improving photocatalytic activity and selectivity for NO oxidation, and presents a mechanism of Z-scheme photocatalytic reaction for NO oxidation.

2. Experimental

2.1 Materials

Zirconium tetrachloride ($ZrCl_4$), N,N-dimethyl formamide (DMF), glacial acetic acid (HAc), and methanol were obtained from Sinopharm Chemical Reagent Co., Ltd. $Na_2WO_4 \cdot 2H_2O$ and $Bi(NO_3)_3 \cdot 5H_2O$ were purchased from Aladdin Industrial Corporation. 2-NH_2-terephthalic acid was procured from Sigma-Aldrich Chemistry. All the reagents were of analytical grade and were used without further purification.

2.2 Synthesis

2.2.1 Synthesis of NH_2-UiO-66. NH_2-UiO-66 was synthesized in accordance with a procedure reported in the literature.[32] In a typical synthesis, $ZrCl_4$ (0.136 g, 0.585 mmol) and 2-NH_2-terephthalic acid (0.106 g, 0.585 mmol) were dissolved in DMF (130 mL) containing 15.6 mL HAc, and the solution was transferred to a 200 mL Teflon-lined stainless steel autoclave. The autoclave was sealed and heated in an oven at 120 °C for 24 h under autogenous pressure. Until it cooled naturally to room temperature, the solid particles were obtained via filtration with a mixture of methanol and DMF (v/v = 1 : 4) to remove residual DMF. The obtained pale yellow product was dried in vacuum at 90 °C for 12 h.

2.2.2 Synthesis of Bi_2WO_6/NH_2-UiO-66. The Bi_2WO_6/NH_2-UiO-66 composites were synthesized via a simple one-step solvothermal method.[28] In detail, $Na_2WO_4 \cdot 2H_2O$ (0.142 g, 0.430 mmol) was dissolved in deionized water (60 mL), vigorously stirring at room temperature. A series of different Bi_2WO_6/NH_2-UiO-66 mass ratios of 1 : 0.5, 1 : 1, 1 : 2, 1 : 3, and 1 : 5 was obtained by adding 0.15 g, 0.30 g, 0.60 g, 0.90 g, and 1.20 g, respectively, of NH_2-UiO-66 to the Na_2WO_4 solution, and the resultant mixtures were stirred for 0.5 h. Then, $Bi(NO_3)_3 \cdot 5H_2O$ (0.417 mg, 0.860 mmol) was added to DMF (60 mL) to form a homogenous white solution. Subsequently, the reaction precursor was stirred for 1 h. And then, it was transferred to a 200 mL Teflon-lined stainless steel autoclave, where the reaction proceeded at 120 °C for 12 h. After naturally cooling, the final products were collected by centrifugation, washed with deionized water, and dried at 60 °C for 12 h. According to the Bi_2WO_6/NH_2-UiO-66 mass ratios, the samples were denoted as BWO/xNU; the labels BWO/0.5NU, BWO/NU, BWO/2NU, BWO/3NU, and BWO/5NU, correspond to Bi_2WO_6/NH_2-UiO-66 mass ratios of 1 : 0.5, 1 : 1, 1 : 2, 1 : 3, and 1 : 5, respectively.

2.3 Characterization

The crystal phases of the samples were observed via X-ray diffraction (XRD) with Cu Kα radiation (Shimadzu XRD-6000, Japan). The morphologies and structures of the catalysts were characterized using a scanning electron microscopy (SEM, SU-8010, Hitachi, Japan) and a transmission electron microscopy (TEM, H-9500, HITACHI, Japan). The N_2 adsorption/desorption isotherms were collected on an N_2 adsorption apparatus (JW-BK 132F, Beijing JWGB Sci & Tech Co., China) and used the Brunauer–Emmett–Teller (BET) method. The pore size distribution was acquired via the Barrett–Joyner–Halenda (BJH) desorption

method. X-ray photoelectron spectroscopy (XPS) experiments were carried out on an XPS instrument (ESCALAB 250Xi, Thermo, USA) to investigate the surface chemical compositions. The binding energies were referenced to C 1s at 284.8 eV. To explore the light absorption properties, the ultraviolet-visible light diffuse reflection spectra (UV-vis DRS) were obtained using a UV-vis diffuse reflection spectrophotometer (Lambda 750 S, PerkinElmer, USA) with a spectral range 200–800 nm. The electron spin resonance (ESR) signals of spin-trapped radicals were detected using a JES FA200 spectrometer (JEOL Ltd., Japan). The photoluminescence spectra were obtained using a fluorescence spectrometer (FLS920, Edinburgh Instruments, England) and the excitation source used was a laser source emitting at 380 nm. The photocurrent, electrochemical AC impedance, and the parameters required for Mott–Schottky plots were measured using an electrochemical workstation (CHI 660E, China). And standard three-electrode system and 0.2 M Na_2SO_4 aqueous solution as the electrolyte are necessary for the electrochemical workstation.

2.4 Photocatalytic activity tests

The photocatalytic activity for NO removal was performed at room temperature in a continuous-flow stainless steel rectangular reactor. There are five channels in the reactor, and photocatalyst (50 mg) was dispersed uniformly on five glass slides, which were placed in the channels. The light source for photocatalytic reaction used a 500 W Xenon lamp (CEL-LAX500, Beijing AuLight Tech Co., Ltd, China), equipped with a 420 nm UV cut-off filter. The NO gas used in the tests was continuously obtained from a NO compressed gas cylinder (50 ppm, N_2 balance). Air stream was used to dilute the concentration of NO to around 500 ppb. Simultaneously, air steam was delivered through a bubbler to adjust the relative humidity (RH) of the reaction gas to 55%. The volume flow rate of the reaction gas was about 0.8 L min^{-1}, with corresponding residence time being 18.75 s. NO adsorption–desorption equilibrium should be achieved before switching on the Xe lamp with a current of 7 A. The concentrations of NO, NO_2, and NO_x

were recorded using an online analyzer (NO–NO$_2$–NO$_x$ Analyzer, Model 42i, Thermo Scientific). Based on the following formulae, NO and NO$_x$ removal efficiencies could be calculated.

$$NO \text{ removal} = (NO_{in} - NO_{out})/NO_{in},$$

$$NO_2 \text{ formation} = NO_{x,out} - NO_{out},$$

where $NO_{in/out}$ represent the concentrations of NO at the inlet and outlet, respectively. And $NO_{x,in/out}$ has the similar meaning.

3. Results and discussion

3.1 Crystal phases and structures

To confirm the phases and crystal structures of pure NH_2-UiO-66, Bi_2WO_6, and the BWO/xNU nanocomposites with different mass ratios of NH_2-UiO-66, the catalysts were characterized via XRD. The XRD results are shown in Fig. S1† and 1a. The XRD patterns of pure NH_2-UiO-66 are consistent with those reported previously,[26,28,32,33] while pristine Bi_2WO_6 shows the characteristic peaks ascribed to russellite (JCPDS: 79-2020). After combining Bi_2WO_6 with NH_2-UiO-66, similar XRD patterns at 2θ = 5–10° are observed in all of the as-prepared catalysts, which are ascribed to NH_2-UiO-66.[26,28,32,33] Compared with those of pure NH_2-UiO-66, the characteristic peaks of BWO/xNU at low angles become weaker as the Bi_2WO_6 content increases. What is noteworthy in Fig. 1b is that the diffraction peaks shift to lower angles at 2θ = 7–9°. According to Bragg's law, the negative shift can be ascribed to the lattice expansion of NH_2-UiO-66 in the hybrids.[34] Moreover, no other impurity peaks can be seen, which indicates that the BWO–NU heterojunctions are successfully obtained and BWO/xNU is a two-phase composite.[35]

The samples's SEM images are shown in Fig. 2. As illustrated in Fig. 2a, pure NH_2-UiO-66 displays a regular octahedral cubic morphology with clean and smooth surfaces and its size is approximately 200–500 nm. Pristine Bi_2WO_6 exhibits nanoparticle-like morphology (Fig. 2d). Interestingly, after the Bi_2WO_6 loading process, the NH_2-UiO-66's surface from BWO/
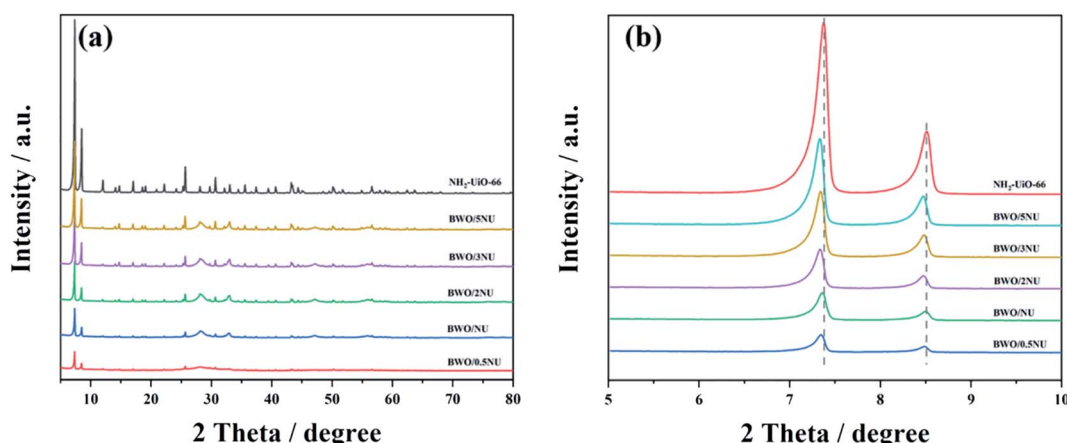
Fig. 1 (a) XRD patterns of NH$_2$-UiO-66 and BWO/xNU samples, and (b) diffraction peaks of pure NH$_2$-UiO-66 and of BWO/xNU ascribed to NH$_2$-UiO-66.
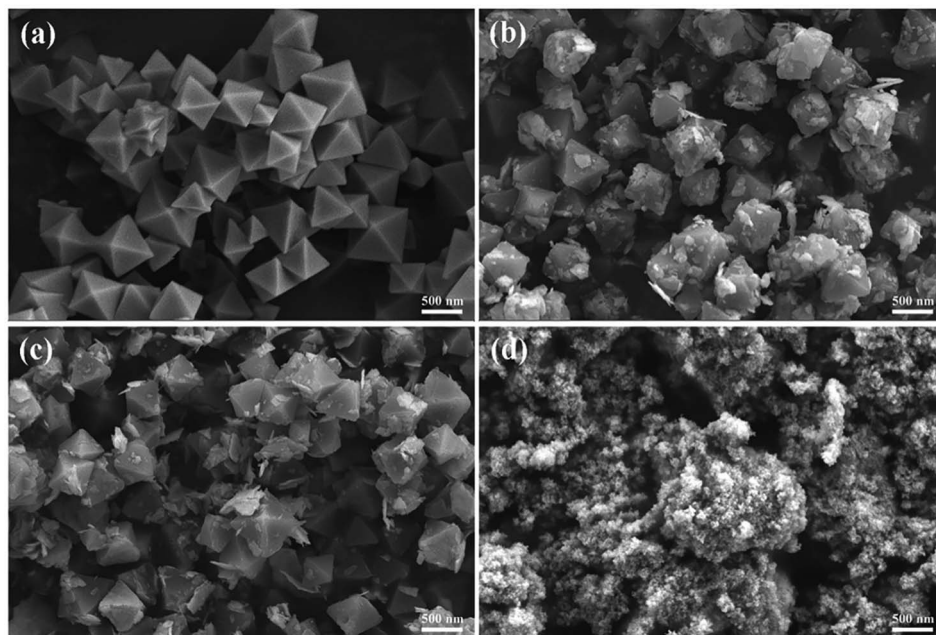
Fig. 2 (a) SEM patterns of NH$_2$-UiO-66 samples, (b and c) SEM patterns of BWO/2NU samples, and (d) SEM patterns of Bi$_2$WO$_6$ samples.

2NU hybrid becomes rough (Fig. 2b and c). In the SEM patterns of BWO/2NU (Fig. 2b and c), large number of nanoplates insert among the NH$_2$-UiO-66 nanocubes. We believe that these nanoplates are Bi$_2$WO$_6$, introduced by the addition of NH$_2$-UiO-66 during the growth of Bi$_2$WO$_6$. To further confirmation, TEM and energy dispersive spectroscopy (EDS) analyses were conducted. These Bi$_2$WO$_6$ nanoplates decorate and disperse on the surface of NH$_2$-UiO-66.

The morphology and structure of samples were additionally analyzed *via* TEM and high-resolution TEM (HRTEM). It is shown in Fig. 3a that pure NH$_2$-UiO-66 has a cube-like morphology, of which size is approximately 200–500 nm. The results are in accordance with the SEM analysis. After hybridization with Bi$_2$WO$_6$ (Fig. 3b and c), the NH$_2$-UiO-66 in the BWO/2NU hybrids can still be observed. Meanwhile, Bi$_2$WO$_6$ displays a nanoplate-like morphology. Further observations show that NH$_2$-UiO-66 and Bi$_2$WO$_6$ are closely bonded, which is consistent with the XRD and SEM analysis. This structure does benefits to the rapid separation of photo-induced charges between NH$_2$-UiO-66 and Bi$_2$WO$_6$ with improving its photocatalytic activity. Additionally, pristine Bi$_2$WO$_6$ displays the morphology of small nanoparticles (Fig. S2†), which differs from that of Bi$_2$WO$_6$ in the BWO/2NU hybrid. The HRTEM image (Fig. 3d) of as-prepared Bi$_2$WO$_6$ shows clear fringes. And lattice spacings of 0.248 nm and 0.255 nm are measured, which can be assigned to the (115) and (022) planes of russellite Bi$_2$WO$_6$, respectively. The EDS spectrum (Fig. 3e and f) confirms that the BWO/2NU hybrid contains elements including Zr, Bi, W, C, N, and O.

The N$_2$ adsorption–desorption measurements were performed to explore the BET surface areas and pore structures of the as-prepared photocatalysts. The results are shown in Fig. 4. NH$_2$-UiO-66 has a large surface area (673.58 m^2 g^{-1}) and its isotherm is of type I, which indicates that the NH$_2$-UiO-66

sample has a microporous structure.[36–38] The BET surface area of pure Bi$_2$WO$_6$ is 52.67 m^2 g^{-1} (Fig. 4), which is relatively low. Moreover, the isotherm of pure Bi$_2$WO$_6$ has a H3 type hysteresis loop, indicating its mesoporous structure. The BET surface areas of BWO/2NU and BWO/0.5NU are 685.41 m^2 g^{-1} and 313.20 m^2 g^{-1}, respectively (Fig. 4). After the combination of Bi$_2$WO$_6$ and NH$_2$-UiO-66, the specific surface areas of different samples increase with decrease in the content of Bi$_2$WO$_6$. It's worth noting that the N$_2$ adsorption–desorption isotherms of all the hybrids present obvious hysteresis loops, revealing the formation of a mesoporous structure in NH$_2$-UiO-66 after the hybridization of Bi$_2$WO$_6$. The combination of micropores and mesopores can be further confirmed using the pore size distributions (Fig. S3 and S4†). Photocatalysts with higher BET surface areas can be expected to produce more active sites for photocatalytic reaction and exhibit improved photocatalytic performance.

The XPS spectra of the as-prepared NH$_2$-UiO-66, Bi$_2$WO$_6$, and BWO/2NU samples were obtained to further clarify the interfacial interaction between NH$_2$-UiO-66 and Bi$_2$WO$_6$. The XPS survey spectrum (Fig. S5†) reveals that the BWO/2NU hybrid is composed of Zr, Bi, W, O, N, and C, which is consistent with the results of EDS. The characteristic peaks of the four elements with different valence states are ascribed to Zr 3d$^{5/2}$ and Zr 3d$^{3/2}$ (Fig. 5a), N 1s (Fig. 5b), Bi 4f$^{7/2}$ and Bi 4f$^{5/2}$ (Fig. 5c), and W 4f$^{7/2}$ and W 4f$^{5/2}$ (Fig. 5d). Compared with those of pure NH$_2$-UiO-66, the high-resolution XPS spectra of Zr 3d$^{5/2}$ and Zr 3d$^{3/2}$ in BWO/2NU shift to lower binding energies by approximately 0.1 eV. It is noticeable that the shift in the binding energies of N 1s exhibits a similar result, indicating strong interfacial interaction between NH$_2$-UiO-66 and Bi$_2$WO$_6$.[15] Meanwhile, the characteristic peaks of Bi 4f$^{7/2}$ and Bi 4f$^{5/2}$, and of W 4f$^{7/2}$ and W 4f$^{5/2}$, attributed to the BWO/2NU hybrid, exhibit positive shifts of
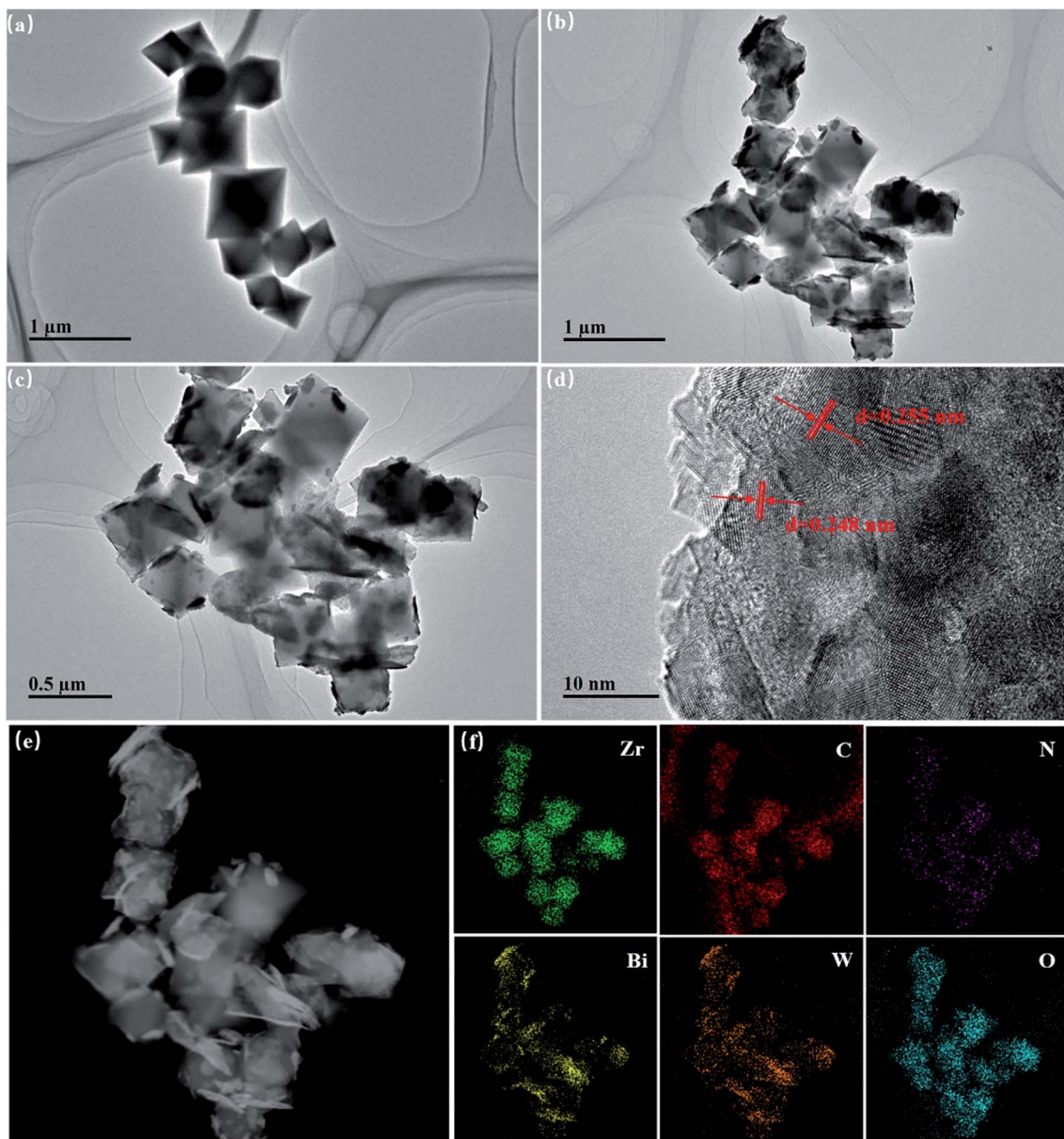
Fig. 3 TEM image of (a) NH_2-UiO-66 samples, (b and c) BWO/2NU samples, (d) HRTEM image of Bi_2WO_6 samples, and (e and f) EDS elemental mapping images of BWO/2NU samples.

0.2 eV and 0.3 eV, when compared with those observed for pure Bi_2WO_6. The shifts in the binding energy of a specific element suggest the electron migration from Bi_2WO_6 to NH_2-UiO-66 with the formation of a built-in electric field at the interface in the direction from Bi_2WO_6 to NH_2-UiO-66 and a strong interfacial interaction between them.

3.2 Photocatalytic activities for NO removal

NO is chosen as the target pollutant to assess the photocatalytic performance of photocatalysts. An adsorption–desorption equilibrium between the test samples and NO was attained before the latter were irradiated using the Xe lamp. Fig. 6a shows that the blank test with no photocatalysts is not active for photocatalytic NO oxidation and the NO concentrations of the

as-prepared samples decrease with increase in illumination time. The maximum NO removal ratio of pure NH_2-UiO-66 is 63% but that of pristine Bi_2WO_6 is only 29%. Moreover, the time taken to achieve stable efficiency is longer in the case of NH_2-UiO-66 and Bi_2WO_6 than in the case of the hybrids. As the NH_2-UiO-66 content increases, the optimal activities of the as-prepared BWO/xNU (x = 0.5, 1, 2, 3, 5) hybrids assume an inverted V-shaped trend. When the NH_2-UiO-66 content of BWO/xNU is 66.7%, the BWO/2NU exhibits an optimum NO removal efficiency of 79%, which is an increase of 272.41% and 118.44% over those achieved with pristine Bi_2WO_6 and NH_2-UiO-66, respectively. It is interesting that the compounds, especially BWO/2NU, could achieve a state of balance rapidly, i.e., in only a few minutes. The photocatalytic NO oxidation of
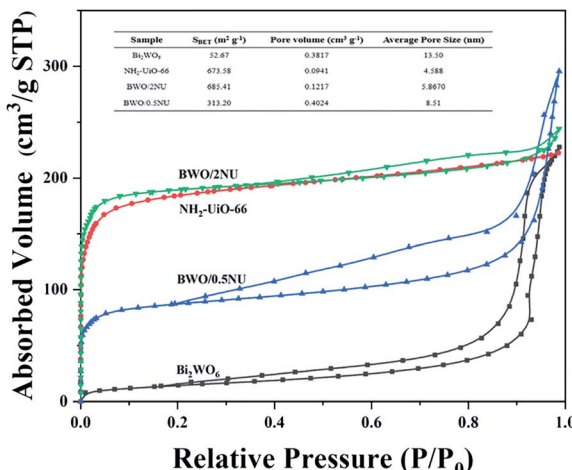
Fig. 4 N_2 adsorption−desorption isotherms and BET surface areas (inset table) of Bi_2WO_6, NH_2-UiO-66, BWO/0.5NU, and BWO/2NU.

different catalysts displays small error variety (error bar < 5%) (Fig. S7†). And Table S1† shows other reported works in the field of photocatalytic NO removal. Among them, the BWO/2NU hybrid displays superior performance.

NO_3^- is the desired product[39] during the photocatalytic oxidation of NO, while NO_2, as one of the reaction intermediates, is not desired. The formation of NO_2 can be used to estimate the product selectivity and photooxidation ability of the materials.[39] Therefore, the NO_2 formation was detected online

and the results are shown in Fig. 6b. It is noteworthy that the NO_2 formation in the case of BWO/xNU hybrids decreases dramatically and is as low as 1.97 ppb when BWO/2NU is used. This quantity can reach 67.89 ppb and 56.22 ppb in the case of pristine Bi_2WO_6 and NH_2-UiO-66, respectively, after stabilization. The above results indicate that the BWO/2NU hybrids are beneficial to the conversion of NO to NO_3^-/NO_2^- owing to their superior oxidation ability.

In addition, stability is usually used as an index to estimate the usefulness of photocatalysts in practical applications. Five-cycle experiments were performed to investigate the BWO/2NU's stability (Fig. 6c). After the first four runs, the efficiency of NO removal decreases slightly with increase in irradiation time. When the photocatalysts were washed with deionized water after four runs, their photocatalytic activity remained nearly unchanged. It is suggested in the literature[40,41] that photocatalytic activity is weakened by the accumulation of HNO_3/HNO_2 on the surfaces of the catalysts, as the active sites of the as-prepared samples are likely covered. However, the powder XRD patterns (Fig. S6†) of the BWO/2NU hybrid used for photocatalysis shows no distinct differences in comparison with a fresh specimen, indicating no structural changes.

3.3 Enhanced mechanism of visible-light photocatalytic activities

To further investigate the enhanced photocatalytic activities, steady-state photoluminescence (PL) spectroscopy, time-resolved photoluminescence (TRPL) spectroscopy, photocurrent, and
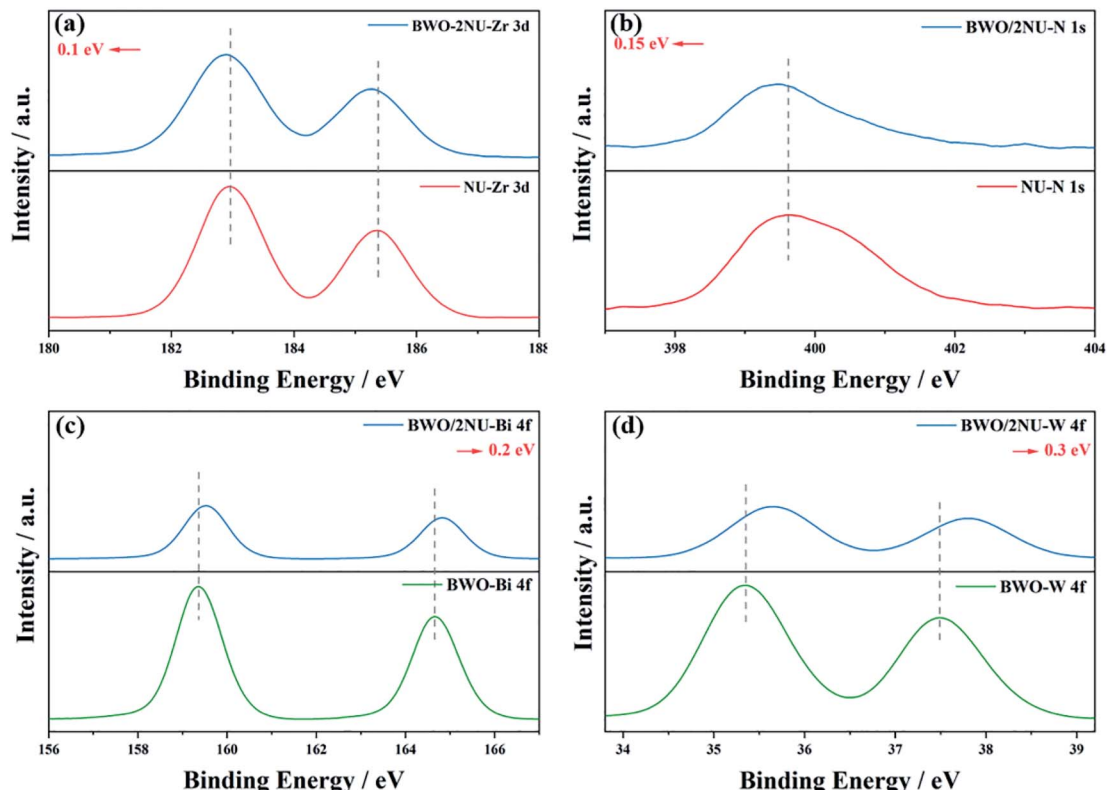
Fig. 5 XPS spectra of (a) Zr 3d, (b) N 1s, (c) Bi 4f, and (d) W 4f.
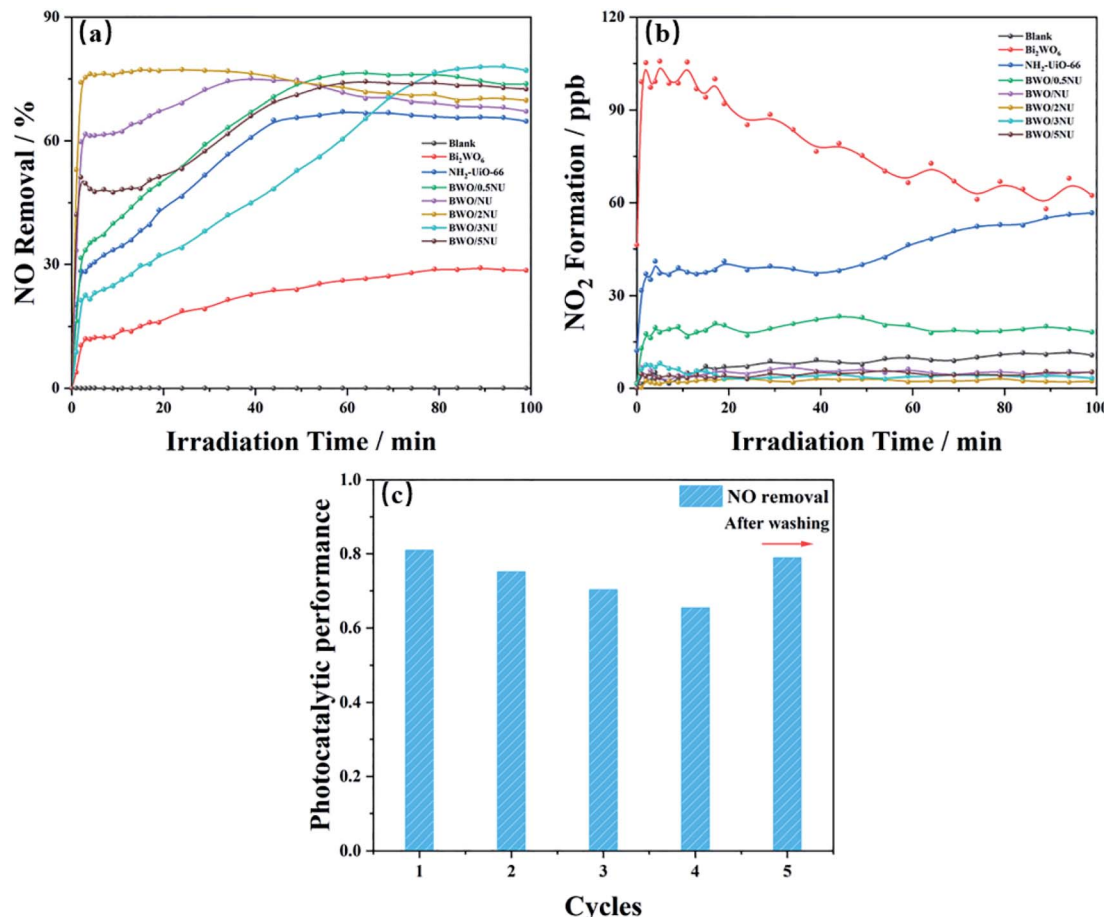
Fig. 6 (a) NO removal efficiencies, and (b) quantities of NO$_2$ formation using different as-prepared samples; and (c) consecutive cycles of photocatalytic reaction of NO on BWO/2NU.

electrochemical impedance spectroscopy (EIS) analyses were performed. The PL emission can be utilized to investigate the recombination of photo-induced electron–hole pairs.[42] The PL spectrum of pure NH$_2$-UiO-66 (Fig. 7a) reveals an emission peak centered at 450 nm. And the PL emission peak of the BWO/2NU hybrid is significantly weaker than that of pure NH$_2$-UiO-66, indicating efficient charge separation between Bi$_2$WO$_6$ and NH$_2$-UiO-66. Fig. 7b presents the TRPL spectra of Bi$_2$WO$_6$, NH$_2$-UiO-66, BWO/0.5NU, and BWO/2NU. Multiexponential decay is observed from the plot. The cubic exponential models were adopted to fit the decay spectra and obtain three radiative lifetimes with different percentages (inset of Fig. 7b). The three lifetimes (τ_1, τ_2, and τ_3) of the BWO/2NU hybrid are all 0.452 ns, which is shorter than the corresponding lifetimes of pristine Bi$_2$WO$_6$ and NH$_2$-UiO-66. Moreover, the BWO/2NU hybrid has a shorter average fluorescence lifetime (0.452 ns) than those of pure Bi$_2$WO$_6$ (0.962 ns) and NH$_2$-UiO-66 (0.602 ns). The recombination of free excitons can lead to a longer lifetime. Therefore, the obvious quenching of all the lifetimes in the transients for BWO/2NU hybrid leads to a shorter decay lifetime, which indicates that interfacial electrons transfer faster at the BWO/2NU hybrid, otherwise charges will recombine and result in enhanced photoluminescence. The above result can be responsible for BWO/2NU's higher photocatalytic performance owing to

the efficient repressed recombination of charges in Bi$_2$WO$_6$ and NH$_2$-UiO-66. The spectra of the transient photocurrent response and electrochemical impedance spectroscopy were analyzed to investigate the separation efficiency of electron–hole pairs. Fig. 7c provides the transient photocurrent responses of Bi$_2$WO$_6$, NH$_2$-UiO-66, BWO/0.5NU, and BWO/2NU under discontinuous visible light irradiation. When the light is switch on, the intensity of photocurrent response for pristine Bi$_2$WO$_6$ or NH$_2$-UiO-66 is weak. After the incorporation of NH$_2$-UiO-66 into Bi$_2$WO$_6$, both BWO/0.5NU and BWO/2NU hybrids show stronger photocurrent intensity than pristine Bi$_2$WO$_6$ or NH$_2$-UiO-66. Generally, the transient photocurrent responses have positive correlations with the separation efficiency of electron–hole pairs, so the above result indicates more efficient separation of photo-induced charges and transfer over the BWO/2NU hybrid.[43] As shown in Fig. 7d, BWO/2NU shows smaller diameter of the arc radius on the Nyquist plot compared with that of pristine Bi$_2$WO$_6$ or NH$_2$-UiO-66, suggesting a considerably smaller charge transfer resistance between the interface of Bi$_2$WO$_6$ and NH$_2$-UiO-66.[44] That is to say the BWO/2NU hybrid has higher efficiency of photo-induced charge separation and migration.[45] All the results reveal that the BWO/2NU hybrid has superior performance of the electron–hole separation and migration than the single component, leading to enhanced photocatalytic abilities.
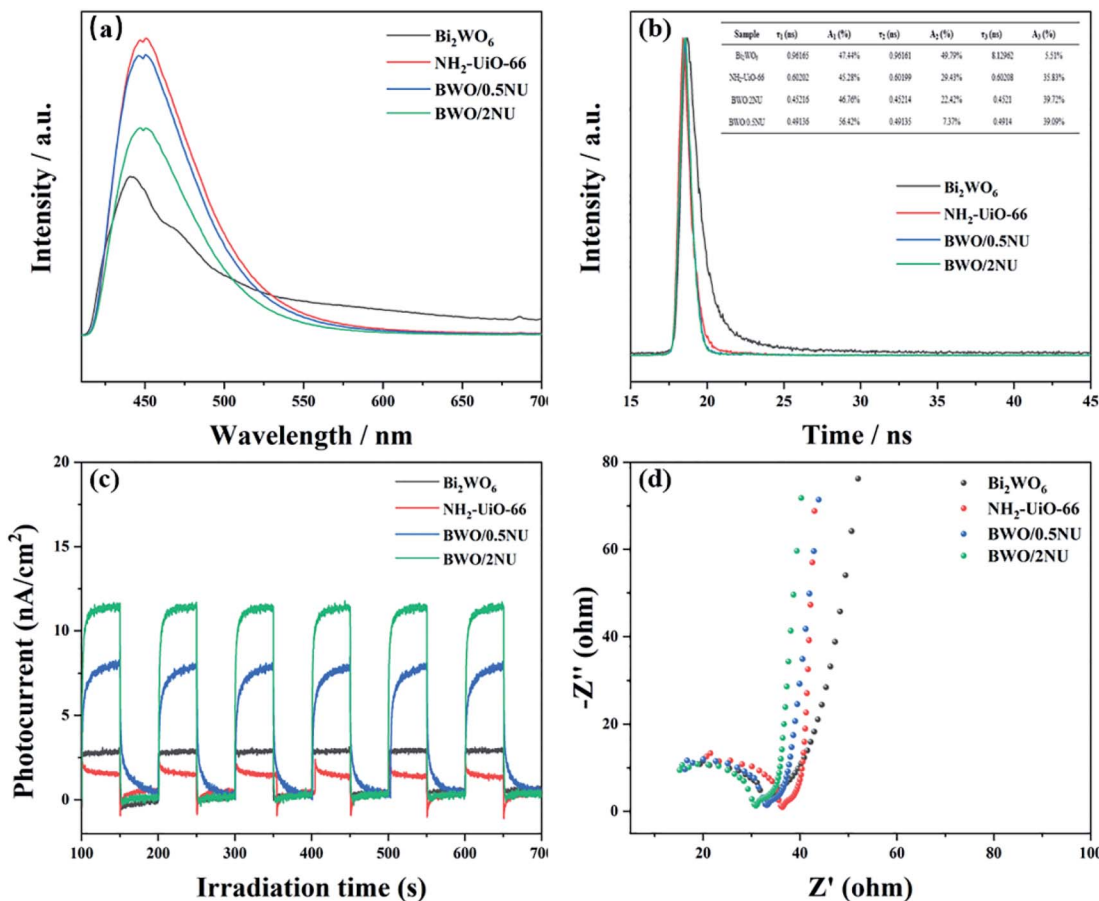
Fig. 7 (a) Stable state PL, and (b) TRPL spectra, (c) photocurrent responses, and (d) EIS images of Bi_2WO_6, NH_2-UiO-66, BWO/0.5NU and BWO/2NU.

Additional experiments were carried out to investigate the detailed band structures/positions of the photocatalysts. The UV-vis DRS analysis (Fig. 8) reveals that pristine Bi_2WO_6 holds an absorption edge of 440 nm, which is close to the reported values.[46,47] NH_2-UiO-66 exhibits strong absorption in the range 200–440 nm.[26] When compared with those of pure Bi_2WO_6 and NH_2-UiO-66, the absorption edges of the hybrids occur with a slight red shift and the BWO/2NU sample shows the strongest response in the visible region, indicating the production of more electron–hole pairs and thereby enhanced photocatalytic performance.[26] The equation, $\alpha h\nu = A(h\nu - E_g)^{n/2}$,[36,48] is used to calculate the band gaps of pristine Bi_2WO_6 and NH_2-UiO-66, where α, h, ν, A, and E_g stand for the absorption coefficient, Planck's constant, optical frequency, a constant, and the band gap, i.e., highest occupied molecular orbital-lowest unoccupied molecular orbital (HOMO–LUMO) gap, respectively. N's values depend on the types of optical transitions in different semiconductors. Hence, the values obtained are $n = 4$ for Bi_2WO_6 (indirect semiconductor) and $n = 1$ for NH_2-UiO-66 (direct semiconductor).[36,49] From the plots of $(\alpha h\nu)^{2/n}$ versus $h\nu$ (Fig. S8†), the band gaps/HOMO–LUMO gaps of the as-prepared Bi_2WO_6 and NH_2-UiO-66 samples are determined to 2.82 eV and 2.86 eV, respectively. Moreover, the HOMO–LUMO gap of the BWO/2NU hybrid is estimated to be 2.80 eV from the absorption edge in Fig. 8. The result suggests that the BWO/2NU hybrid is not a simple mixture of Bi_2WO_6 and NH_2-UiO-66, but entails the formation of an interfacial interaction, which indicates the formation of a heterojunction structure.

It's demonstrated in Fig. 9 that the CBs of Bi_2WO_6, NH_2-UiO-66, and BWO/2NU were determined using the Mott–Schottky method.
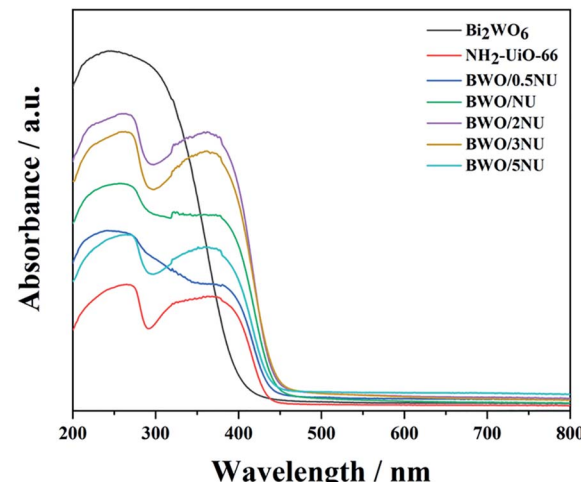
Fig. 8 UV-vis DSR spectra of as-prepared samples.
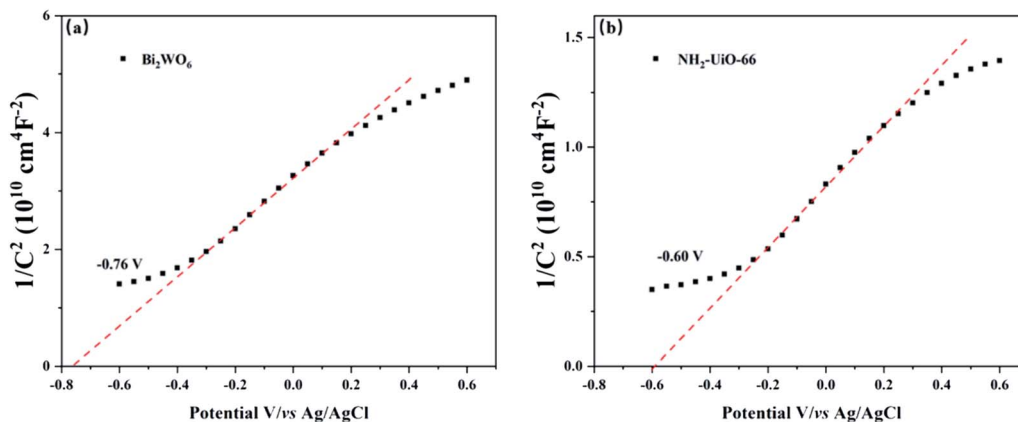
Fig. 9 Mott–Schottky plots for (a) Bi_2WO_6, and (b) NH_2-UiO-66.

The slopes of the Mott–Schottky curves are positive, indicating that both Bi_2WO_6 and NH_2-UiO-66 are n-type semiconductors.[26] The flat-band potentials of Bi_2WO_6 and NH_2-UiO-66 are approximately -0.76 V vs. Ag/AgCl (i.e., -0.56 V vs. normal hydrogen electrode (NHE)) and -0.60 V vs. Ag/AgCl (i.e., -0.40 V vs. NHE), respectively. Generally, the flat band potential is about 0–0.2 V below the bottom of the CB in n-type semiconductors.[50] Here, the voltage difference between the CB and flat band potential was set to 0.1 eV.[50] Therefore, the CB positions of Bi_2WO_6 and NH_2-UiO-66 can be calculated to be -0.66 V and -0.50 V (vs. NHE), respectively. By combining these results with the band gap values of the as-prepared photocatalysts derived from the UV-vis DRS analysis (Fig. 8), the VB positions of Bi_2WO_6 and NH_2-UiO-66 are determined to be $+2.16$ V and $+2.36$ V (vs. NHE), respectively.

To confirm and investigate the mechanism of the Z-scheme BWO/2NU system, the ESR spin-trap (with 5,5-dimethyl-1-pyrroline N-oxide (DMPO)) was employed. Fig. 10 shows that no characteristic peaks of $\cdot$OH or $\cdot O_2^-$ are observed in pristine Bi_2WO_6, NH_2-UiO-66, and the BWO/0.5NU, BWO/2NU, and BWO/5NU hybrids without irradiation. Under visible light irradiation (Fig. 10a), strong ESR signals corresponding to the DMPO-$\cdot O_2^-$ adduct are clearly observed for both pristine Bi_2WO_6 and the BWO/xNU hybrids, whereas no signal is

observed in the case of pure NH_2-UiO-66. Moreover, the signals of DMPO-$\cdot O_2^-$ attributed to the hybrids are generally much stronger than those in the case of pristine Bi_2WO_6. As depicted in Fig. 10b, the DMPO-$\cdot$OH signals of the BWO/xNU hybrids are detected under visible light irradiation but not in the case of pure Bi_2WO_6 or NH_2-UiO-66. The above results suggest that the BWO/xNU hybrids, with Bi_2WO_6 incorporated into the NH_2-UiO-66 catalysts, can produce more active radicals, thereby enhancing photocatalytic activity.

Based on the UV-vis DRS analysis and Mott–Schottky plots, the VB/CB (HOMO/LUMO) positions of Bi_2WO_6 and NH_2-UiO-66 are determined to be $+2.16/-0.66$ V and $+2.36/-0.5$ V (vs. NHE), respectively. The CB potential of Bi_2WO_6 (-0.66 V vs. NHE) is more negative than the standard potential of $O_2/\cdot O_2^-$ (-0.33 V vs. NHE),[51] and hence, the $\cdot O_2^-$ generated by Bi_2WO_6 can be detected. In addition, the CB potential of NH_2-UiO-66 (-0.5 V vs. NHE) is more negative than that of $O_2/\cdot O_2^-$, but no $\cdot O_2^-$ signal is observed in the case of pure NH_2-UiO-66, which is probably owing to the production of a few DMPO-$\cdot O_2^-$ adducts. Meanwhile, the HOMO energy of NH_2-UiO-66 is higher than the potential energy of $H_2O/\cdot$OH (2.27 V vs. NHE),[52] but $\cdot$OH was not generated for reasons similar to those mentioned above. Bi_2WO_6 has lower VB potential and hence, the production of
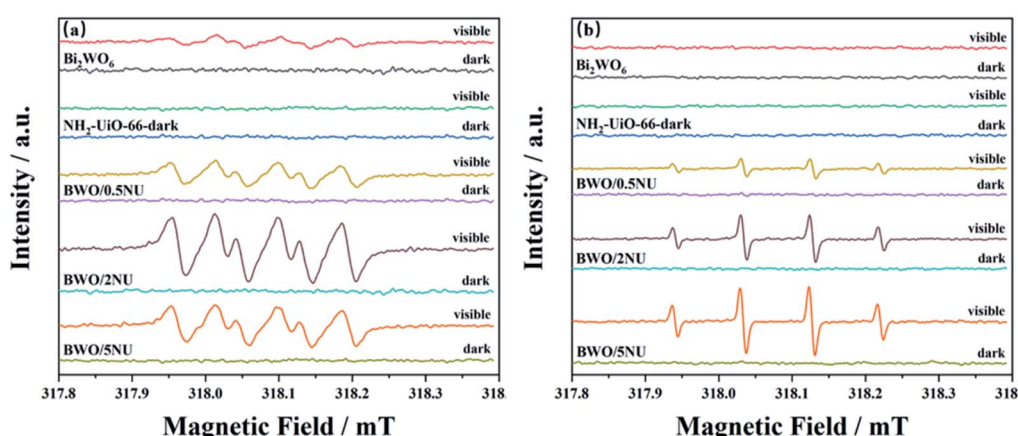
**Fig. 10** DMPO spin-trapping ESR spectra for (a) DMPO-$\cdot O_2^-$, and (b) DMPO-$\cdot$OH$^-$.
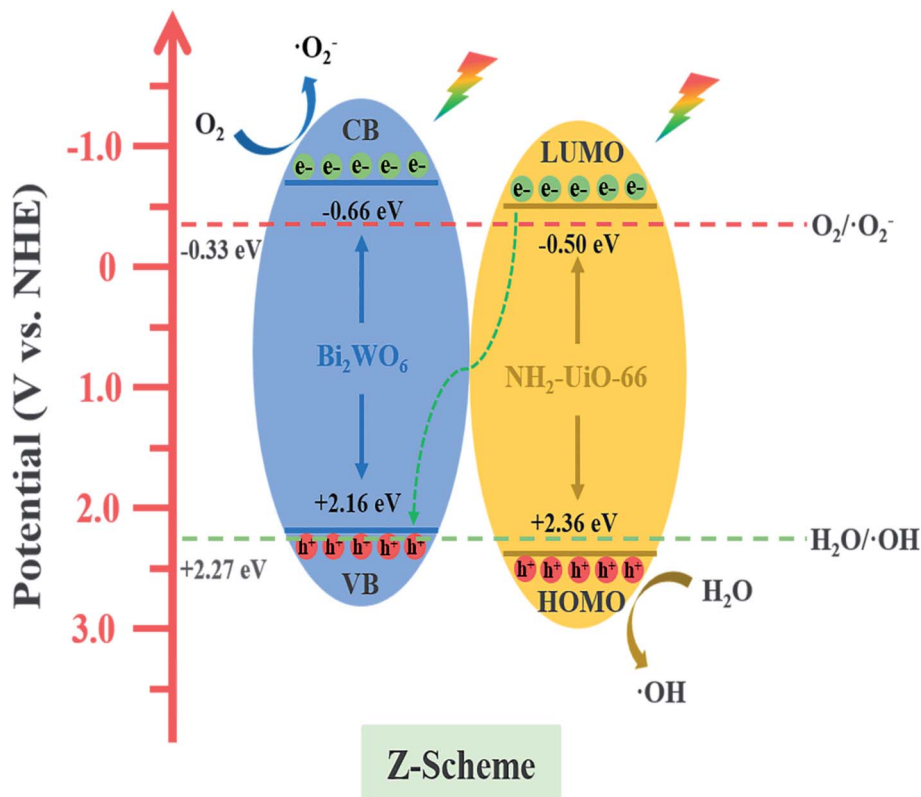
Fig. 11 Schematic diagram of direct Z-scheme system for photocatalysis and charge migration pathway.

·OH is prohibited. Both ·O$_2^-$ and ·OH signals are observed in the case of the BWO/xNU hybrids. Therefore, a direct Z-scheme photocatalytic system is proposed, which is displayed in Fig. 11.

Moreover, the potential E_F (Fermi level) of pristine Bi$_2$WO$_6$ is about −0.89 eV (vs. SCE),[23] negative than that of pure NH$_2$-UiO-66 about −0.58 eV (vs. SCE).[53] When the Bi$_2$WO$_6$ and the NH$_2$-UiO-66 get into contact, the electrons will migrate from the surface of Bi$_2$WO$_6$ to the surface of NH$_2$-UiO-66 to achieve their Fermi level equilibrium.[16] After Fermi level equilibrium is achieved, the region close to the interface of BWO/xNU is charged, which results in the formation of a built-in electric field in the direction from Bi$_2$WO$_6$ to NH$_2$-UiO-66.

The photo-induced electrons from the CB of NH$_2$-UiO-66 transfer to the interface and combine with the photo-induced holes on the VB of Bi$_2$WO$_6$. In addition, the formation of the built-in electric field pointing from Bi$_2$WO$_6$ to NH$_2$-UiO-66 will accelerate the electron transfer from the LUMO of NH$_2$-UiO-66 to the VB of Bi$_2$WO$_6$. This promotes the accumulation of electrons on the CB of Bi$_2$WO$_6$ and of holes on the VB of NH$_2$-UiO-66, resulting in the preservation of the strong reducibility of electrons and strong oxidation ability of holes. The direct Z-scheme photocatalytic mechanism proposed is in excellent agreement with the results of ESR analysis.

4. Conclusion

In this study, a novel direct Z-scheme photocatalytic system composed of NH$_2$-UiO-66 and Bi$_2$WO$_6$ for efficient NO oxidation

under visible light irradiation was proposed. The incorporation of NH$_2$-UiO-66 into Bi$_2$WO$_6$ can not only effectively improve its photocatalytic activity for NO oxidation, but also increase the selectivity for converting NO to NO$_3^-$/NO$_2^-$, truly diminishing the potential secondary pollution of NO$_2$. The introduction of NH$_2$-UiO-66 produces abundant active sites to promote the adsorption and photocatalytic reaction. Meanwhile, combining NH$_2$-UiO-66 with Bi$_2$WO$_6$ can narrow the band gaps of the hybrids to some extent to enhance their light adsorption. The fabrication of a direct Z-scheme system improves the separation efficiency of electron–hole pairs. Simultaneously it preserves their strong redox abilities. This work provides a new idea for the construction of a direct Z-scheme photocatalytic system without cocatalysts for NO photocatalytic removal. We hope this work can provide some inspiration on the design and synthesis of more advanced photocatalysts for environmental protection.

Conflicts of interest

There are no conflicts to declare.

Acknowledgements

References

1 Y. Feng, L. Ling, J. Nie, K. Han, X. Chen, Z. Bian, H. Li and Z. L. Wang, Self-Powered Electrostatic Filter with Enhanced Photocatalytic Degradation of Formaldehyde Based on Built-in Triboelectric Nanogenerators, *ACS Nano*, 2017, **11**, 12411–12418.

2 F. Wang, Z. Xie, J. Liang, B. Fang, Y. Piao, M. Hao and Z. Wang, Tourmaline-Modified FeMnTiO$_x$ Catalysts for Improved Low-Temperature NH$_3$-SCR Performance, *Environ. Sci. Technol.*, 2019, **53**, 6989–6996.

3 J. Angelo, L. Andrade, L. M. Madeira and A. Mendes, An overview of photocatalysis phenomena applied to NO$_x$ abatement, *J. Environ. Manage.*, 2013, **129**, 522–539.

4 F. Rezaei, A. A. Rownaghi, S. Monjezi, R. P. Lively and C. W. Jones, SO$_x$/NO$_x$ Removal from Flue Gas Streams by Solid Adsorbents: A Review of Current Challenges and Future Directions, *Energy Fuels*, 2015, **29**, 5467–5486.

5 S. Xiong, J. Weng, Y. Liao, B. Li, S. Zou, Y. Geng, X. Xiao, N. Huang and S. Yang, Alkali Metal Deactivation on the Low Temperature Selective Catalytic Reduction of NO$_x$ with NH$_3$ over MnO$_x$-CeO$_2$: A Mechanism Study, *J. Phys. Chem. C*, 2016, **120**, 15299–15309.

6 A. Wang, Y. Guo, F. Gao and C. H. F. Peden, Ambient-temperature NO oxidation over amorphous CrO$_x$-ZrO$_2$ mixed oxide catalysts: Significant promoting effect of ZrO$_2$, *Appl. Catal., B*, 2017, **202**, 706–714.

7 G. Jiang, X. Li, M. Lan, T. Shen, X. Lv, F. Dong and S. Zhang, Monodisperse bismuth nanoparticles decorated graphitic carbon nitride: Enhanced visible-light-response photocatalytic NO removal and reaction pathway, *Appl. Catal., B*, 2017, **205**, 532–540.

8 Y. Huang, Y. Liang, Y. Rao, D. Zhu, J. J. Cao, Z. Shen, W. Ho and S. C. Lee, Environment-Friendly Carbon Quantum Dots/ ZnFe$_2$O$_4$ Photocatalysts: Characterization, Biocompatibility, and Mechanisms for NO Removal, *Environ. Sci. Technol.*, 2017, **51**, 2924–2933.

9 J. Ma, H. He and F. Liu, Effect of Fe on the photocatalytic removal of NO over visible light responsive Fe/TiO$_2$ catalysts, *Appl. Catal., B*, 2015, **179**, 21–28.

10 Z.-F. Huang, J. Song, X. Wang, L. Pan, K. Li, X. Zhang, L. Wang and J.-J. Zou, Switching charge transfer of C$_3$N$_4$/ W$_{18}$O$_{49}$ from type-II to Z-scheme by interfacial band bending for highly efficient photocatalytic hydrogen evolution, *Nano Energy*, 2017, **40**, 308–316.

11 X. Chen, H. Zhang, D. Zhang, Y. Miao and G. Li, Controllable synthesis of mesoporous multi-shelled ZnO microspheres as efficient photocatalysts for NO oxidation, *Appl. Surf. Sci.*, 2018, **435**, 468–475.

12 Y. Luan, L. Jing, Y. Xie, X. Sun, Y. Feng and H. Fu, Exceptional Photocatalytic Activity of 001-Facet-Exposed TiO$_2$ Mainly Depending on Enhanced Adsorbed Oxygen by Residual Hydrogen Fluoride, *ACS Catal.*, 2013, **3**, 1378–1385.

13 J. Cao, J. Zhang, X. a. Dong, H. Fu, X. Zhang, X. Lv, Y. Li and G. Jiang, Defective borate-decorated polymer carbon nitride: Enhanced photocatalytic NO removal, synergy effect and reaction pathway, *Appl. Catal., B*, 2019, **249**, 266–274.

14 J. Zhang, Y. Hu, X. Jiang, S. Chen, S. Meng and X. Fu, Design of a direct Z-scheme photocatalyst: preparation and characterization of Bi$_2$O$_3$/g-C$_3$N$_4$ with high visible light activity, *J. Hazard. Mater.*, 2014, **280**, 713–722.

15 Z. Jiang, W. Wan, H. Li, S. Yuan, H. Zhao and P. K. Wong, A Hierarchical Z-Scheme alpha-Fe$_2$O$_3$/g-C$_3$N$_4$ Hybrid for Enhanced Photocatalytic CO$_2$ Reduction, *Adv. Mater.*, 2018, **30**, 1706108.

16 J. Low, B. Dai, T. Tong, C. Jiang and J. Yu, In Situ Irradiated X-Ray Photoelectron Spectroscopy Investigation on a Direct Z-Scheme TiO$_2$/CdS Composite Film Photocatalyst, *Adv. Mater.*, 2019, **31**, 1802981.

17 T. Di, B. Zhu, B. Cheng, J. Yu and J. Xu, A direct Z-scheme g-C$_3$N$_4$/SnS$_2$ photocatalyst with superior visible-light CO$_2$ reduction performance, *J. Catal.*, 2017, **352**, 532–541.

18 W. Yu, D. Xu and T. Peng, Enhanced photocatalytic activity of g-C$_3$N$_4$ for selective CO$_2$ reduction to CH$_3$OH via facile coupling of ZnO: a direct Z-scheme mechanism, *J. Mater. Chem. A*, 2015, **3**, 19936–19947.

19 J. Low, C. Jiang, B. Cheng, S. Wageh, A. A. Al-Ghamdi and J. Yu, A Review of Direct Z-Scheme Photocatalysts, *Small Methods*, 2017, **1**, 1700080.

20 M. Zhu, Z. Sun, M. Fujitsuka and T. Majima, Z-Scheme Photocatalytic Water Splitting on a 2D Heterostructure of Black Phosphorus/Bismuth Vanadate Using Visible Light, *Angew. Chem., Int. Ed. Engl.*, 2018, **57**, 2160–2164.

21 J. Yu, S. Wang, J. Low and W. Xiao, Enhanced photocatalytic performance of direct Z-scheme g-C$_3$N$_4$-TiO$_2$ photocatalysts for the decomposition of formaldehyde in air, *Phys. Chem. Chem. Phys.*, 2013, **15**, 16883–16890.

22 H. Zhou, Z. Wen, J. Liu, J. Ke, X. Duan and S. Wang, Z-scheme plasmonic Ag decorated WO$_3$/Bi$_2$WO$_6$ hybrids for enhanced photocatalytic abatement of chlorinated-VOCs under solar light irradiation, *Appl. Catal., B*, 2019, **242**, 76–84.

23 S. Luo, J. Ke, M. Yuan, Q. Zhang, P. Xie, L. Deng and S. Wang, CuInS$_2$ quantum dots embedded in Bi$_2$WO$_6$ nanoflowers for enhanced visible light photocatalytic removal of contaminants, *Appl. Catal., B*, 2018, **221**, 215–222.

24 J. Zhang, X. Yuan, L. Jiang, Z. Wu, X. Chen, H. Wang, H. Wang and G. Zeng, Highly efficient photocatalysis toward tetracycline of nitrogen doped carbon quantum dots sensitized bismuth tungstate based on interfacial charge transfer, *J. Colloid Interface Sci.*, 2018, **511**, 296–306.

25 J. Hu, D. Chen, Z. Mo, N. Li, Q. Xu, H. Li, J. He, H. Xu and J. Lu, Z-Scheme 2D/2D Heterojunction of Black Phosphorus/ Monolayer Bi$_2$WO$_6$ Nanosheets with Enhanced Photocatalytic Activities, *Angew. Chem., Int. Ed. Engl.*, 2019, **58**, 2073–2077.

26 J. Meng, Q. Chen, J. Lu and H. Liu, Z-Scheme Photocatalytic CO$_2$ Reduction on a Heterostructure of Oxygen-Defective ZnO/Reduced Graphene Oxide/UiO-66-NH$_2$ under Visible Light, *ACS Appl. Mater. Interfaces*, 2019, **11**, 550–562.

27 L. Shen, S. Liang, W. Wu, R. Liang and L. Wu, CdS-decorated UiO–66(NH$_2$) nanocomposites fabricated by a facile photodeposition process: an efficient and stable visible-light-driven photocatalyst for selective oxidation of alcohols, *J. Mater. Chem. A*, 2013, **1**, 11473.

28 Z. Sha, J. Sun, H. S. On Chan, S. Jaenicke and J. Wu, Bismuth tungstate incorporated zirconium metal–organic framework composite with enhanced visible-light photocatalytic performance, *RSC Adv.*, 2014, **4**, 64977–64984.

29 Z. Sha and J. Wu, Enhanced visible-light photocatalytic performance of BiOBr/UiO-66(Zr) composite for dye degradation with the assistance of UiO-66, *RSC Adv.*, 2015, **5**, 39592–39600.

30 R. Wang, L. Gu, J. Zhou, X. Liu, F. Teng, C. Li, Y. Shen and Y. Yuan, Quasi-Polymeric Metal-Organic Framework UiO-66/g-C$_3$N$_4$ Heterojunctions for Enhanced Photocatalytic Hydrogen Evolution under Visible Light Irradiation, *Adv. Mater. Interfaces*, 2015, **2**, 1500037.

31 C. Gomes Silva, I. Luz, F. X. Llabres i Xamena, A. Corma and H. Garcia, Water stable Zr-benzenedicarboxylate metal-organic frameworks as photocatalysts for hydrogen generation, *Chem.–Eur. J.*, 2010, **16**, 11133–11138.

32 X. Wang, W. Chen, L. Zhang, T. Yao, W. Liu, Y. Lin, H. Ju, J. Dong, L. Zheng, W. Yan, X. Zheng, Z. Li, X. Wang, J. Yang, D. He, Y. Wang, Z. Deng, Y. Wu and Y. Li, Uncoordinated Amine Groups of Metal-Organic Frameworks to Anchor Single Ru Sites as Chemoselective Catalysts toward the Hydrogenation of Quinoline, *J. Am. Chem. Soc.*, 2017, **139**, 9419–9422.

33 S.-T. Gao, W. Liu, C. Feng, N.-Z. Shang and C. Wang, A Ag–Pd alloy supported on an amine-functionalized UiO-66 as an efficient synergetic catalyst for the dehydrogenation of formic acid at room temperature, *Catal. Sci. Technol.*, 2016, **6**, 869–874.

34 H. Huang, K. Liu, K. Chen, Y. Zhang, Y. Zhang and S. Wang, Ce and F Comodification on the Crystal Structure and Enhanced Photocatalytic Activity of Bi$_2$WO$_6$ Photocatalyst under Visible Light Irradiation, *J. Phys. Chem. C*, 2014, **118**, 14379–14387.

35 H. Cheng, J. Hou, O. Takeda, X.-M. Guo and H. Zhu, A unique Z-scheme 2D/2D nanosheet heterojunction design to harness charge transfer for photocatalysis, *J. Mater. Chem. A*, 2015, **3**, 11006–11013.

36 Y. Su, Z. Zhang, H. Liu and Y. Wang, Cd$_{0.2}$Zn$_{0.8}$S@UiO-66-NH$_2$ nanocomposites as efficient and stable visible-light-driven photocatalyst for H$_2$ evolution and CO$_2$ reduction, *Appl. Catal., B*, 2017, **200**, 448–457.

37 Z. Hu, Y. Peng, Z. Kang, Y. Qian and D. Zhao, A Modulated Hydrothermal (MHT) Approach for the Facile Synthesis of UiO-66-Type MOFs, *Inorg. Chem.*, 2015, **54**, 4862–4868.

38 Y. Han, M. Liu, K. Li, Y. Zuo, Y. Wei, S. Xu, G. Zhang, C. Song, Z. Zhang and X. Guo, Facile synthesis of morphology and size-controlled zirconium metal–organic framework UiO-66: the role of hydrofluoric acid in crystallization, *CrystEngComm*, 2015, **17**, 6434–6440.

39 Y. Zhou, X. Zhang, Q. Zhang, F. Dong, F. Wang and Z. Xiong, Role of graphene on the band structure and interfacial interaction of Bi$_2$WO$_6$/graphene composites with enhanced photocatalytic oxidation of NO, *J. Mater. Chem. A*, 2014, **2**, 16623–16631.

40 G. Li, D. Zhang and J. Yu, A new visible-light photocatalyst: CdS quantum dots embedded mesoporous TiO$_2$, *Environ. Sci. Technol.*, 2009, **43**, 7079–7085.

41 C. H. Ao and S. C. Lee, Enhancement effect of TiO$_2$ immobilized on activated carbon filter for the photodegradation of pollutants at typical indoor air level, *Appl. Catal., B*, 2003, **44**, 191–205.

42 W. Zhong, S. Shen, S. Feng, Z. Lin, Z. Wang and B. Fang, Facile fabrication of alveolate Cu$_{2-x}$Se microsheets as a new visible-light photocatalyst for discoloration of Rhodamine B, *CrystEngComm*, 2018, **20**, 7851–7856.

43 W. Zhong, W. Tu, S. Feng and A. Xu, Photocatalytic H$_2$ evolution on CdS nanoparticles by loading FeSe nanorods as co-catalyst under visible light irradiation, *J. Alloys Compd.*, 2019, **772**, 669–674.

44 W. Zhong, Z. Lin, S. Feng, D. Wang, S. Shen, Q. Zhang, L. Gu, Z. Wang and B. Fang, Improved oxygen evolution activity of IrO$_2$ by in situ engineering of an ultra-small Ir sphere shell utilizing a pulsed laser, *Nanoscale*, 2019, **11**, 4407–4413.

45 W. Zhong, S. Shen, M. He, D. Wang, Z. Wang, Z. Lin, W. Tu and J. Yu, The pulsed laser-induced Schottky junction via in situ forming Cd clusters on CdS surfaces toward efficient visible light-driven photocatalytic hydrogen evolution, *Appl. Catal., B*, 2019, **258**, 117967.

46 Z. Zhang, W. Wang, L. Wang and S. Sun, Enhancement of visible-light photocatalysis by coupling with narrow-band-gap semiconductor: a case study on Bi$_2$S$_3$/Bi$_2$WO$_6$, *ACS Appl. Mater. Interfaces*, 2012, **4**, 593–597.

47 Y. Tian, B. Chang, J. Lu, J. Fu, F. Xi and X. Dong, Hydrothermal synthesis of graphitic carbon nitride-Bi$_2$WO$_6$ heterojunctions with enhanced visible light photocatalytic activities, *ACS Appl. Mater. Interfaces*, 2013, **5**, 7079–7085.

48 L. Zhang, W. Wang, Z. Chen, L. Zhou, H. Xu and W. Zhu, Fabrication of flower-like Bi$_2$WO$_6$ superstructures as high performance visible-light driven photocatalysts, *J. Mater. Chem.*, 2007, **17**, 2526.

49 Z. Wang, T. Hu, K. Dai, J. Zhang and C. Liang, Construction of Z-scheme Ag$_3$PO$_4$/Bi$_2$WO$_6$ composite with excellent visible-light photodegradation activity for removal of organic contaminants, *Chin. J. Catal.*, 2017, **38**, 2021–2029.

50 Y. Wang, Y. Zeng, X. Chen, Q. Wang, L. Guo, S. Zhang and Q. Zhong, One-step hydrothermal synthesis of a novel 3D BiFeWO$_x$/Bi$_2$WO$_6$ composite with superior visible-light photocatalytic activity, *Green Chem.*, 2018, **20**, 3014–3023.

51 W. He, Y. Sun, G. Jiang, H. Huang, X. Zhang and F. Dong, Activation of amorphous Bi$_2$WO$_6$ with synchronous Bi metal and Bi$_2$O$_3$ coupling: Photocatalysis mechanism and reaction pathway, *Appl. Catal., B*, 2018, **232**, 340–347.

52 H. Huang, Y. He, X. Li, M. Li, C. Zeng, F. Dong, X. Du, T. Zhang and Y. Zhang, Bi$_2$O$_2$(OH)(NO$_3$) as a desirable [Bi$_2$O$_2$]$^{2+}$ layered photocatalyst: strong intrinsic polarity, rational band structure and {001} active facets co-beneficial for robust photooxidation capability, *J. Mater. Chem. A*, 2015, **3**, 24547–24556.

53 X. Wang, X. Zhao, D. Zhang, G. Li and H. Li, Microwave irradiation induced UIO-66-NH$_2$ anchored on graphene with high activity for photocatalytic reduction of CO$_2$, *Appl. Catal., B*, 2018, **228**, 47–53.